Materials Science & Engineering A 784 (2020) 139323

Contents lists available at ScienceDirect

Materials Science & Engineering A

journal homepage: http://www.elsevier.com/locate/msea

Lattice-distortion dependent yield strength in high entropy alloys

Li Li [a], Qihong Fang [a,*], Jia Li [a,**], Bin Liu [b], Yong Liu [b], Peter K. Liaw [c]

[a] State Key Laboratory of Advanced Design and Manufacturing for Vehicle Body, Hunan University, Changsha, 410082, PR China
[b] State Key Laboratory for Powder Metallurgy, Central South University, Changsha, 410083, PR China
[c] Department of Materials Science and Engineering, The University of Tennessee, Knoxville, TN, 37996, USA

ARTICLE INFO

Keywords:
High-entropy alloys
Lattice distortion effect
Solute concentration
Solid-solution strengthening
Yield strength

ABSTRACT

High entropy alloys (HEAs) have attracted great attention due to their impressive properties induced by the severe lattice distortion in comparison to the conventional alloys. However, the effect of severe lattice distortion on the mechanical properties in face-centered-cubic (FCC) and body-centered-cubic (BCC) structured HEAs is still not fully understood, which are critically important to the fundamental studies as well as the industrial applications. Herein, an analytical model for predicting the solid-solution strengthening and the yield stress in FCC and BCC HEAs accounting for the lattice distortion is presented. Both the calculated solid-solution strengthening and the yield strength are compared to the experimental results, to verify the rationality of the built theoretical model. The numerical predictions considering the severe lattice-distortion effect agree well with the experimental results for both FCC and BCC HEAs, in terms of the yield strength and the solid-solution strengthening. Based on theoretical model, the constructed contour line of solid-solution strengthening can be used to evaluate the effect of elemental type on yield strength of HEAs, which provides guideline for discovering and screening the advanced HEAs. Furthermore, it has been identified the atomic-radius mismatch and solid-solution strengthening do not increase directly as the number of components increases in HEAs based on the theoretical analysis. In the Al_x-Cr-Co-Fe-Ni-Mn HEA system, the atomic-radius mismatch and shear-modulus mismatch induced by the added Al element govern the solid-solution strengthening, but this situation disappears in the Al_x-Hf-Nb-Ta-Ti-Zr HEA system. It is further confirmed that the effect of the atomic-radius mismatch on the solid-solution strengthening is obviously higher than effect of the shear-modulus mismatch, dominating the yield strength. These results provide an insight into the effect of severe lattice distortion on the yield strength, and demonstrate a theoretical framework for identifying the desired compositions to create the excellent HEAs.

1. Introduction

High entropy alloys (HEAs) break the traditional alloy design concepts where the traditional alloys are composed of one or rarely two dominant elements. HEAs are essentially composed of five or more principal elements in equimolar or near-equimolar ratios, with each elemental composition between 5 and 35 atomic percent [1–9]. Even though HEAs possess the complex compositions, they are typically keen on the formation of single solid-solution structures, such as face-centered-cubic (FCC), body-centered-cubic (BCC), or hexagonal-close-packed (HCP) structures, owing to the fact that their high-mixing entropy can decrease the Gibbs free energy and retard the formation of intermetallic [10–15]. The multi-component HEAs have drawn great attention due to their remarkable mechanical potentials, such as outstanding tensile strength and fracture toughness at cryogenic temperatures [16], wonderful thermal stability [17,18], resistance to wear and corrosion [3,7,19,20], and great fatigue and creep properties [2,5,7,10], which conventional metal materials can't afford. These excellent properties qualify that the HEAs can be applied in a wide range of fields.

It is established that the mechanical property of HEAs is strongly dependent on the microstructure. Therefore, recent paper [21–32] are devoted to enhancing the link between the microstructure and performance in HEAs, and improving the mechanical properties by adjusting the microstructure. For example, with various Al and Ti compositions, a series of $Al_xCo_{1.5}CrFeNi_{1.5}Ti_y$ HEAs were designed in the previous work [21]. Compared with the traditional wear-resistant steels, the wear resistance of the $Co_{1.5}CrFeNi_{1.5}Ti$ and $Al_{0.2}Co_{1.5}CrFeNi_{1.5}Ti$ HEAs are at

* Corresponding author.
** Corresponding author.
E-mail addresses: fangqh1327@hnu.edu.cn (Q. Fang), lijia123@hnu.edu.cn (J. Li).

https://doi.org/10.1016/j.msea.2020.139323
Received 9 October 2019; Received in revised form 18 March 2020; Accepted 29 March 2020
Available online 2 April 2020

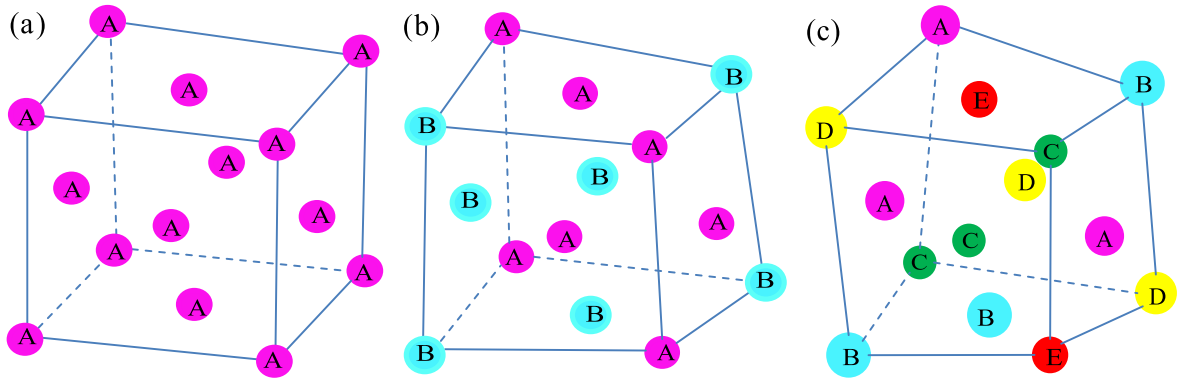

Fig. 1. Schematic illustration of the single FCC crystal structure (a). The prefect crystal cell with only one element (b). The distorted crystal cell due to the addition of the other element with the different atomic size and shear modulus (c). The distorted crystal for five-principal-element HEAs, the size and color of the circles represent the differently-incorporated principal elements. (For interpretation of the references to color in this figure legend, the reader is referred to the Web version of this article.)

least two times better with the similar hardness [22]. This trend is attributed to the excellent anti-oxidation property and resistance to thermal softening in HEAs [21]. The valence electron concentration plays an important role in phase formation, based on the valence electron concentration, an effective method is proposed to design HEA constituents for balancing strength and ductility by selecting ideal elements [23], it is found high valence electron concentration is beneficial to forming FCC phases that improve ductility, while a low valence electron concentration is conducive in forming BCC phases with enhanced strength. By making use of the state-of-the-art TEM characterization technique, dislocation reactions in a plastically-deformed FCC HEA was conducted [24]. It is found the low stacking fault energy results in the widely-dissociated dislocation cores, which, subsequently, causes the significant work hardening with a large hardening rate. In addition, the effect of the temperature on the stacking fault energy for FeCrCoNiMn has been studied in previous research using quantum mechanical first-principles methods [25]. The results show a large positive temperature factor for the stacking fault energy, which could explain the observed twinning induced plasticity effect at sub-zero temperatures and the transformation induced plasticity effect at cryogenic conditions in FeCrCoNiMn [25]. Moreover, the molecular-dynamics simulation is also employed in studying the plastic-deformation mechanism of HEAs in recent years. The kinetics of the strain-induced phase transformation from FCC to BCC phases in the single-crystal and nanocrystalline HEA is investigated in the previous work, it is found that the low stacking fault energy plays a key role in affecting the plasticity of HEA [26]. Combining elasticity-based theory and material inputs computed by ab initio methods, a predictive theory for the yield strength in FCC HEAs is presented [27,28]. Further, a predictive model on the intrinsic yield strength of HEAs is presented within the framework of the Peierls-Nabarro model [31]. Combining the mechanical testing and the literature data, a solid-solution strengthening model containing the athermal component and the thermally-activated component is developed to describe the yield stress of refractory HEAs [32]. Through different research methods, the previous studies have made a great progress in revealing the close correlation between the microstructures and properties of HEAs [21–32].

Due to the difference in atomic size and shear modulus between different principal elements, noteworthy lattice-distortion are produced in HEAs. It has been demonstrated that the strain in the HEA lattice is greater than that of pure Ni, the magnitude of this strain was similar to that observed in some of the binary Ni–33Cr and ternary Ni-37.5Co–25Cr alloys and cannot be considered anomalously large in previous research [33]. As shown in Figs. 1a and 2a, there is almost no lattice distortion in the perfect FCC and BCC structure with only one element. As the addition of the other element with different atomic size and atomic shear-modulus, the severe lattice distortion occurs in both the binary alloy and the five-principal-element HEAs (see Fig. 1b, c, 2b and 2c). However, the effect of the additional element on the lattice distortion is unclear, and the strengthening mechanism produced by the severe lattice distortion is still not fully understood in theoretical perspectives [34–36].

The purpose of this study is to explore theoretically the severe lattice-distortion effect on the strength of HEAs. In order to achieve this purpose, a theoretical model is developed by introducing the distorted unit cell. Moreover, the grain-size distribution effect is coupled in the present proposed model to more precisely predict the yield strength. The proposed model is applied to describe the severe lattice-distortion effect and predict the yield strength of HEAs. The numerical predictions are in good agreement with the experimental results in terms of both the yield strength and the solid-solution strengthening in various HEAs. Furthermore, the impacts of the Al atomic fraction on the solid-solution strengthening and mismatch degree in the Al_x-Co-Cr-Fe-Ni-Mn and Al_x-Hf-Nb-Ta-Ti-Zr HEAs are discussed. The present research demonstrate that the atomic-radius mismatch in HEAs and medium-entropy alloys are not significant but similar to that in binary alloys theoretically. The contour plots on the shear modulus and atomic radius effects in solid-solution strengthening of various HEAs can provide help for discovering and screening the high strength of advanced HEAs. The meaningful model is expected to provide a theoretical method to explore the severe lattice-distortion effect and discover advanced higher-strength HEAs in the future.

2. Theoretical analysis

2.1. Lattice-distortion effect

As is known to all, the solid-solution strengthening of metals and alloys originates from the elastic interactions between the local stress fields of solute atoms and the mobile dislocations. In the dilute alloys with a low solute concentration, the solute atoms are almost surrounded by the solvent atoms, resulting in that the local lattice distortions caused by the solute atoms are greatly slight. Hence, the lattice-friction stress is pretty small for the dilute alloys. For the dilute solid solution, a simple expression of the solid-solution strengthening is obtained in the previous study [37,38]. Later on, the solid-solution strengthening in the multiple solute-element alloy system is developed [39]. However, the HEAs are especially extraordinary, compared to the binary alloys and multiple

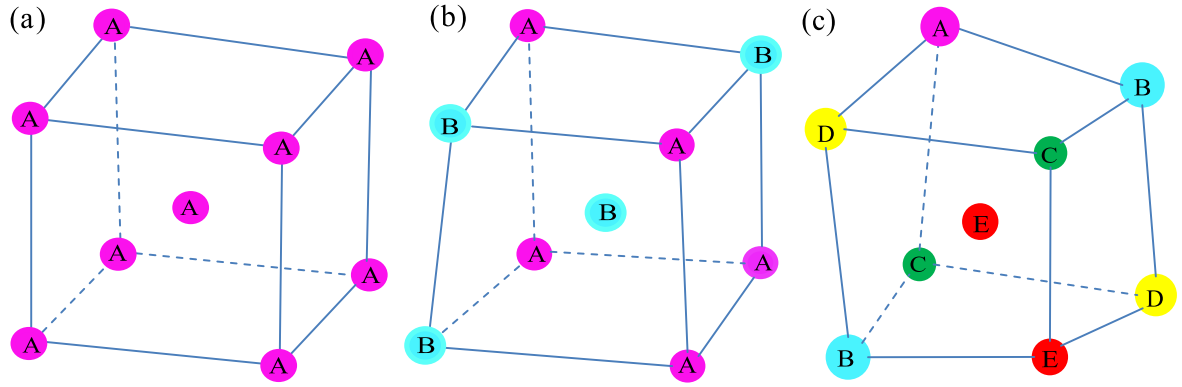

Fig. 2. Schematic illustration of the single BCC crystal structure (a). The prefect crystal cell with only one element (b). The distorted crystal cell with two elements (c). The distorted crystal for five-principal-element HEAs.

solute element alloys, owing to the severe lattice-distortion effect induced by the significant atomic-size difference in the HEAs. Although the solid-solution strengthening mechanism mentioned above is well applicable to the conventional alloys, it may not be perfect for HEAs with the severe lattice distortion. Compared with the traditional alloys, the local stress field caused by the severe lattice distortion in HEAs could strongly impede the movement of the dislocations. The attempts have been made to study the lattice-distortion effect of the BCC HEAs by the means of introducing a distorted BCC unit cell [34]. In view of the above theoretical study on lattice distortion in high-entropy alloys [27,28,34–36,40], the present work is to further explore the lattice distortion from theoretical perspective.

The lattice distortion originates from the elastic mismatch and the atomic size mismatch. According to the previous investigations [34], the elastic mismatch and the atomic-size mismatch between the atoms i and j can be expressed as

$$\delta r_{ij} = 2\left(r_i - r_j\right)/\left(r_i + r_j\right) \tag{1}$$

$$\delta G_{ij} = 2\left(G_i - G_j\right)/\left(G_i + G_j\right) \tag{2}$$

where r_i and r_j represent the atomic radii, G_i and G_j are the shear moduli of pure metal crystals i and j, respectively. Based on the hypothesis that the measured lattice parameter of a solid solution alloy is the average of all the interatomic spacing within a selected region of the lattice, an effective model to predict the composition-related lattice parameters of metallic solid solutions [41]. Hence, we are going to describe the average elastic mismatch and atomic size mismatch in HEAs according to the elastic mismatch and the atomic size mismatch between the atoms i and j. The average elastic mismatch and atomic size mismatch can be expressed as

$$\delta r^{ave} = \sum_i^n \sum_j^n c_i c_j \delta r_{ij} = (c_1, c_2, \cdots, c_n) \begin{pmatrix} \delta r_{11} & \delta r_{12} & \cdots & \delta r_{1n} \\ \delta r_{21} & \delta r_{22} & \cdots & \delta r_{2n} \\ \vdots & \cdots & \ddots & \vdots \\ \delta r_{n1} & \delta r_{n2} & \cdots & \delta r_{nn} \end{pmatrix} \begin{pmatrix} c_1 \\ c_2 \\ \vdots \\ c_n \end{pmatrix} \tag{3}$$

$$\delta G^{ave} = \sum_i^n \sum_j^n c_i c_j \delta G_{ij} = (c_1, c_2, \cdots, c_n) \begin{pmatrix} \delta G_{11} & \delta G_{12} & \cdots & \delta G_{1n} \\ \delta G_{21} & \delta G_{22} & \cdots & \delta G_{2n} \\ \vdots & \cdots & \ddots & \vdots \\ \delta G_{n1} & \delta G_{n2} & \cdots & \delta G_{nn} \end{pmatrix} \begin{pmatrix} c_1 \\ c_2 \\ \vdots \\ c_n \end{pmatrix} \tag{4}$$

where δG_{ij} and δr_{ij} represent the elastic mismatch and the atomic size mismatch between the atoms i and j, as mentioned above in Eqs. (1) and (2). c_i and c_j denote the concentrations (in atomic fraction) of principal element i and j in HEAs, respectively. Since there are no elastic mismatch and atomic size mismatch between the atoms i, δG_{ii} and δr_{ii} are specified as zero. The physical nature of this expression is that the probability of the occurrence of the mismatch between the atoms i and i is $c_i c_i$, while that of between the atom j and atom i is $c_j c_i$ in HEAs. Symmetrically, the probability of the occurrence of the mismatch between the atoms i and j is $c_i c_j$.

Both the average elastic mismatch and atomic size mismatch have been obtained in the above content. Then we are going to probe the mismatch caused by a single element in HEAs. It is assumed that the multi-principal HEAs *ijklm* is composed of multi-principal-matrix *jklm* and the additional element *i*. Hence, the atomic-size mismatch and the elastic mismatch caused by the element *i* in *ijklm* HEA are

$$\delta r_i = \frac{\delta r^{ave}_{ijklm} - \delta r^{ave}_{jklm}}{\delta c_i} \tag{5}$$

$$\delta G_i = \frac{\delta G^{ave}_{ijklm} - \delta G^{ave}_{jklm}}{\delta c_i} \tag{6}$$

where δr^{ave}_{ijklm} and δr^{ave}_{jklm} are calculated by Eq. (3), and δG^{ave}_{ijklm} and δG^{ave}_{jklm} are obtained through Eq. (4), δc_i represents the atomic fraction difference of the element i between the *ijklm* HEA and *jklm* HEA. If the *ijklm* is equimolar HEA with five principal elements, δc_i is equal to 0.2.

According to the previous investigations [34], the expression of the mismatch-parameter-related strengthening introduced by a single element in HEAs can be expressed as

$$\sigma_f^i = AGc_i^{2/3}\delta_i^{4/3} \tag{7}$$

where A is a non-dimensional constant dependent on the materials of the order of 0.04 [36]. G is the shear modulus of the material, and c_i is the atomic fraction of individual principal elements in HEAs. The mismatch parameter, δ_i, in Eq. (7) can be expressed as [37].

$$\delta_i = \xi\left(\delta G_i^2 + \beta^2 \delta r_i^2\right)^{1/2} \tag{8}$$

where the elastic mismatch δG_i and the atomic size mismatch δr_i introduced by element i are obtained through Eqs. (5) and (6). ξ is equal to 1 for FCC metals, and of 2.5 for BCC metals. It is generally believed that $3 < \beta < 16$ for screw dislocation, and $\beta > 16$ for edge dislocation [37]. It is provided β is equal to 16 due to the dominant dislocations are edge type in HEAs. Hence, there is no fitting parameter in present model. According to the Vegard's law, the shear modulus in Eq. (7) is written as

$$G = \sum_i^n c_i G_i \tag{9}$$

Based on the mismatch-parameter-related strengthening introduced by a single element, the solid-solution strengthening in HEAs can be expressed as according to the Vegard's law

$$\sigma_f = \sum c_i \sigma_f^i \tag{10}$$

2.2. Grain-size-distribution effect

The classical grain-boundary-strengthening model relies on the single average size of the grain obtained by experimental observations, which can be described by the classical Hall-Petch strengthening relationship as follows [42].

$$\sigma_{GB} = \frac{k}{\sqrt{d}} \tag{11}$$

where k represents the strengthening coefficient of the material, and d is the average grain diameter.

Most of studies consider that the mean grain size acquired from the transmission-electron microscopy (TEM), X-ray diffraction (XRD), and electron backscatter diffraction (EBSD) can describe the grain characteristic of the alloys. For the purpose of more accurately quantifying the grain-boundary strengthening, the effect of the grain-size distribution is taken in consideration in the present model. According to the previous study [43,44], the grain-size distribution follows a log-normal statistical function. Hence, the probability density function of the grain-size distribution can be written as [43,44].

$$f\left(d\right) = \frac{1}{\sqrt{2\pi}\sigma d}\exp\left[-\frac{\left(\mathrm{In}(d)-\mu\right)^2}{2\sigma^2}\right] \tag{12}$$

where μ and σ are the geometric mean value and the geometric standard deviation of $\mathrm{In}(d)$. The error bars can be obtained by the standard deviation for the geometric mean of the measured grain size as a measure of dispersion. The upper and lower limits of the error bar are equal to $e^{\mu+\sigma}$ and $e^{\mu-\sigma}$, which represent the spread of the large and small grains.

With the consideration of the grain-size distribution, the grain boundary strengthening can be expressed as

$$\sigma_{GB} = \int_0^\infty k d^{-1/2} f(d) dd \tag{13}$$

Here, it is necessary to emphasize that the parameter, d, in Eq. (13) represents the grain with a specific size, rather than the mean grain size, which is a statistical quantity in Eq. (11) for the classical Hall-Petch strengthening relationship. Although the average grain size is a statistical value in the classical Hall-Petch strengthening relationship, the parameter of only the average size of grains is difficult to describe the effect of the size distribution, and cannot accurately measure and evaluate the strength from the contribution of a large number of grains. In Eq. (12), μ and σ are both the statistical quantities, and this method is imperative to more accurately predict the grain-boundary strengthening, as compared with the prediction and assessment of the single parameter from the classical Hall-Petch strengthening relationship.

2.3. Precipitation strengthening

Precipitation strengthening is governed by either the Orowan-bypassing mechanism or the shearing mechanism. One of the two mechanisms has a smaller increment, which is the operative strengthening mechanism. When the precipitate size is larger than the critical size to determinate the operative strengthening mechanism, the precipitates are bypassed by the dislocation through the Orowan mechanism. The critical stress, σ_{pre}, can be expressed according to the classical equation [45].

$$\sigma_{pre} = \frac{0.4MGb}{\pi\sqrt{1-\upsilon}}\frac{\mathrm{In}(2\bar{r}/b)}{L_p} \tag{14}$$

where $M = 3.06$ is the Taylor factor, G is the shear modulus of the material, υ is the Poisson ratio, b is the Burgers vector, $\bar{r} = \sqrt{2/3}\cdot r$ is the mean precipitate radius on the slip plane, and r is the average precipitate radius. L_p is the mean precipitate spacing

$$L_p = \left(\sqrt{\frac{\pi}{4f}} - 1\right)\cdot 2\bar{r} \tag{15}$$

where f is the volume fraction of the precipitates.

Combining the solid-solution strengthening σ_f, the grain-boundary strengthening σ_{GB}, and precipitation strengthening σ_{pre}, the yield stress for HEAs can be expressed as

$$\sigma_y = \sigma_f + \sigma_{GB} + \sigma_{pre} \tag{16}$$

3. Results

3.1. Severe lattice distortion on yield stress in FCC HEA

In order to verify the accuracy and rationality of the model, the predicted tensile strength mentioned above are compared with the experimental results in the $Al_{0.3}CrCoFeNi$ HEA [13]. According to the previous study [46], the Hall-Petch coefficient, k, in the $Al_{0.3}CrCoFeNi$ HEA in Eq. (7) is 824 MPa $\mu m^{0.5}$. As for the solid-solution strengthening based on the constructed theoretical model, the atomic radius and the shear modulus of each element are shown in Table 1. Fig. 3a shows the tensile strength computed by the theoretical model and experimental results. As shown in Fig. 3a, the tensile strengths predicted by our model can match the experimental results very well. The predicted yield stress in the HEA consists of three parts, namely, the grain-boundary-strengthening stress, the solid-solution strengthening caused by the severe lattice distortion, and the precipitation-strengthening stress. The value of the yield stress by the experiments is 1147 MPa [13], and the predicted result from our model is 1128 MPa with a deviation of 1.7%. For the predicted yield stress, the grain-boundary strengthening is 652 MPa, which dominates the yield strength; the solid-solution strengthening caused by the severe lattice distortion is 436 MPa; and the precipitation strengthening is 40 MPa, which accounts for the smallest contribution to the strength of the $Al_{0.3}CrCoFeNi$ HEA [13]. It is necessary to emphasize that the precipitate from the solid solution altering the chemistry of the solid solution, which would produce a certain effect on the solid solution strengthening. By coupling the experiments and the precipitation kinetics modeling, the evolution law of the different strengthening mechanisms during the aging process in aluminum alloy were investigated [47]. It is found that the dislocation strengthening and solid solution strengthening were the main role, and larger than 90% of total strengthening at the beginning of aging ($t < 0.5$ h). With the passing of aging time, precipitate strengthening gradually increased and exceeded the dislocation strengthening before 60 min aging time. Moreover, the effect of the conventional solidification and sub-rapid solidification on the microstructure and mechanical properties of Al–Mg–Si alloy were studied [48]. The results show that Mg atoms are inclined to be trapped in α-Al matrix during sub-rapid solidification, leading to less Mg_2Si phase formed at grain boundaries. But Mg atoms can easily form the Mg_2Si phase during conventional solidification due to the lower cooling rate. Therefore, the competitive relationship between the solid solution strengthening and precipitation strengthening may be dependent on the aging time and cooling rate based on the previous research [47,48]. But the specific chemical composition of precipitate in $Al_{0.3}CrCoFeNi$ HEAs is not clear in previous experimental results [13]. And constructing the precipitate thermodynamics and kinetics models to investigate the

Table 1
The parameter of the constituent elements.

Elements	Co	Cr	Fe	Ni	Al
Atomic radius, r (pm)	125	128	126	124	143
Shear modulus, G (GPa)	75	115	82	76	26
Atomic fraction, c (%)	23.26	23.26	23.26	23.26	6.98

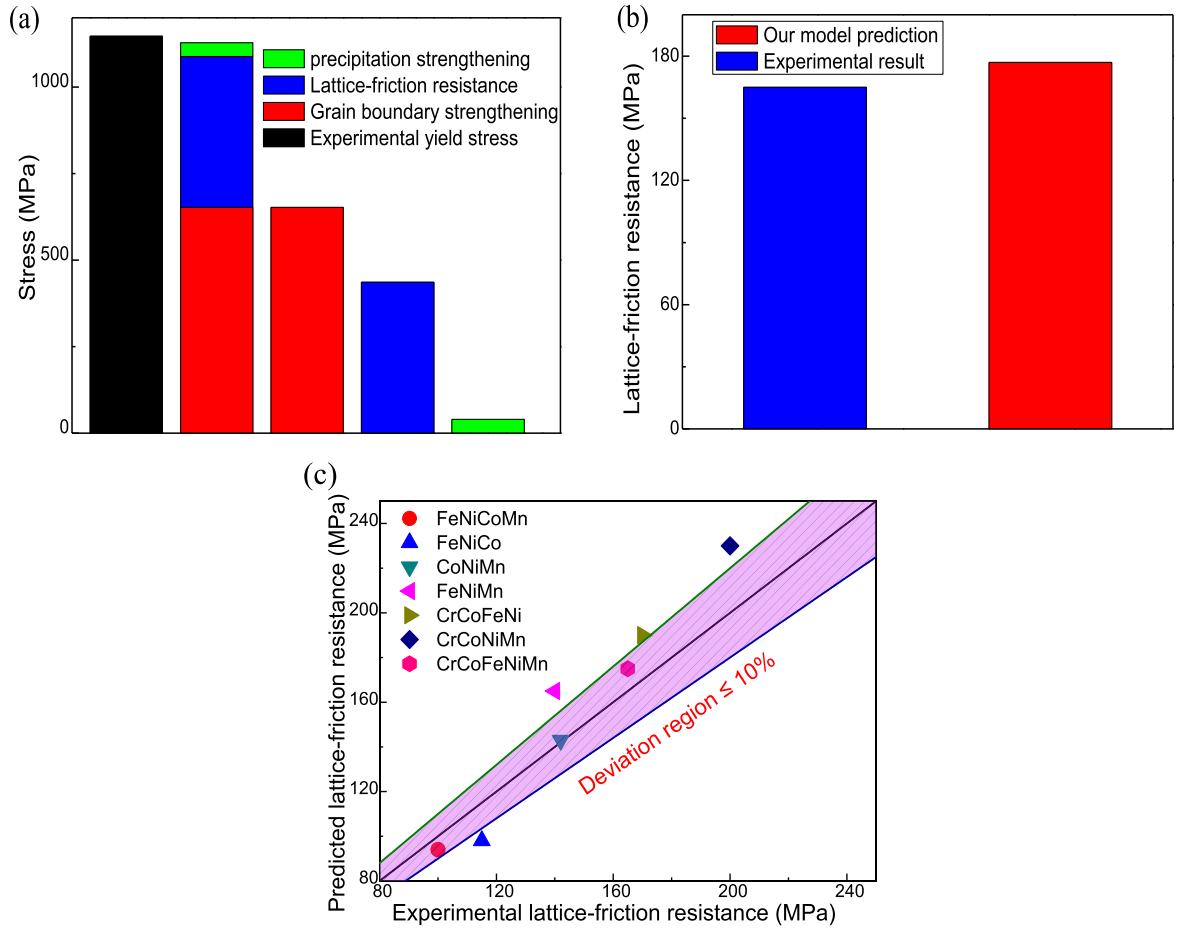

Fig. 3. (a) A comparison in the yield strength from the experimental data and theoretical result, where the yield strength is contributed from the sum of different strengthening mechanisms in $Al_{0.3}$CrCoFeNi HEA [13]. σ_{GB} is the grain-boundary strengthening, σ_f is the solid-solution strengthening, and σ_{pre} is the precipitation strengthening. (b) A comparison in the solid-solution strengthening in CrCoFeNiMn HEA, which is equal to the difference between the yield strength and grain-boundary strengthening, σ_{GB}. (c) The deviation relationship of the solid-solution strengthening between the experimental and predicted results for various FCC HEAs [49]. The pink region means the deviation value less than 10% between the experiment and simulation, and the black line represents the completely consistent relationship of the solid-solution strengthening between the experimental and predicted data. (For interpretation of the references to color in this figure legend, the reader is referred to the Web version of this article.)

evolution of the size, volume fraction and chemical composition of precipitate are not the main work of the current paper. Therefore, the competitive relationship between the solid solution strengthening and the precipitate strengthening is overlooked in our work.

To further confirm the rationality of our theory, we compare our model prediction of the solid-solution strengthening with the

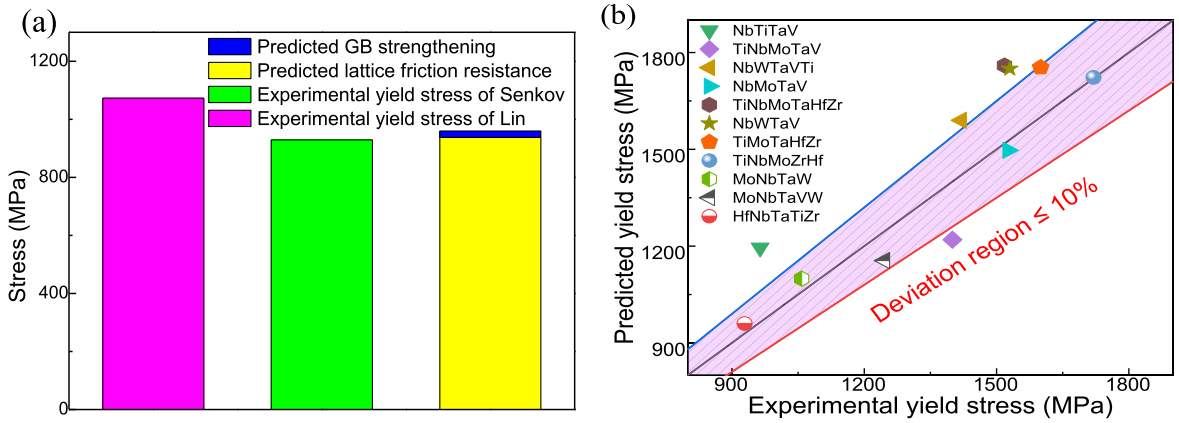

Fig. 4. (a) The comparison of the yield stress between the experimental data and theoretical result for the BCC TaNbHfZrTi HEA. The experimental data of the yield stresses for the TaNbHfZrTi HEA are from Refs. [34,50]. (b) The deviation relationship of the yield stresses between the experimental and predicted data for various BCC HEAs [36]. The pink region means the deviation value less than 10% between the experiment and simulation. (For interpretation of the references to color in this figure legend, the reader is referred to the Web version of this article.)

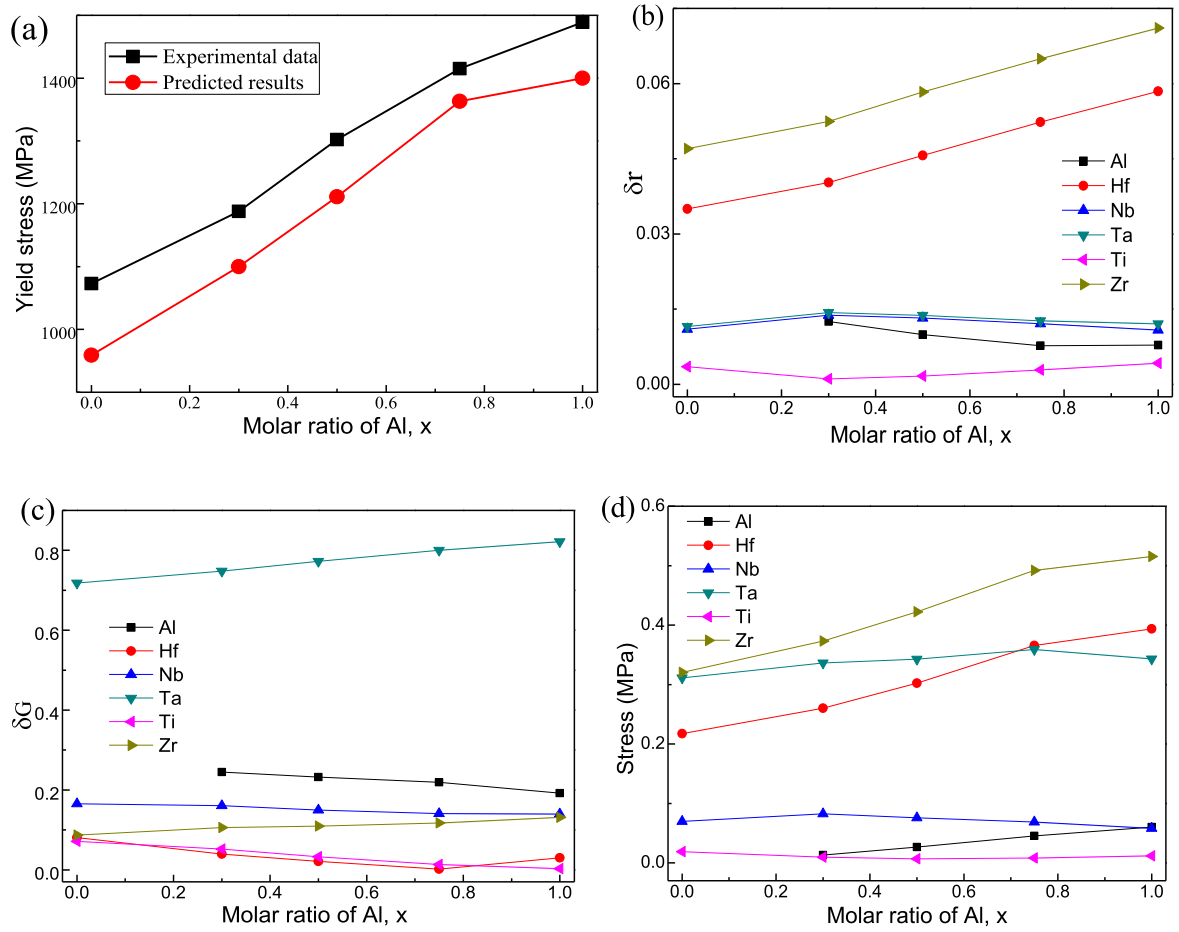

Fig. 5. (a) The relationship between the yield strength and Al composition in the BCC Al_x-Hf-Nb-Ta-Ti-Zr HEAs. (b) The relationship between the atomic-size mismatch and Al composition. (c) The correlation between the shear-modulus mismatch and Al composition. (d) The correlation between the solid-solution strengthening introduced by individual element and Al composition.

experimental data. For the CrCoFeNiMn HEA, the yield strength is mainly contributed by two parts, i.e., the grain-boundary strengthening dependent on the grain size, and the solid-solution strengthening associated with the severe lattice distortion. As shown in Fig. 3b, the solid-solution strengthening predicted by our model is compared to the experimental results measured for the CrCoFeNiMn HEA [46]. Here, the solid-solution strengthening is 165 MPa from the experiment [46], and 177 MPa with a deviation of 7.2% from the simulated results, indicating the predicted value consistent with the experimental results. Fig. 3c exhibits the correlation of the solid-solution strengthening between the experimental data and predicted results in different FCC HEAs [49]. It is apparent that the predictions of the present model can match a majority of the previous experimental data. The deviation value is 7.2% in the CoCrFeNiMn HEA, 15% in the CoCrNiMn HEA, 11.7% in the CrCoFeNi HEA, 6% in the FeNiCoMn HEA, 17.8% in the FeNiMn MEA, 0.7% in the CoNiMn MEA, and 14.7% in the FeNiCo MEA. This trend indicates that the solid-solution strengthening in FCC HEAs varies with the composition. Moreover, the solid-solution strengthening does not increase directly as the number of components increases in the Fe–Co–Ni–Cr–Mn HEA system, agreeing with the previous research [26]. The proposed theoretical model appears to be capable of capturing the main features of the variation in solid-solution strengthening with alloy composition in HEAs.

3.2. Severe lattice distortion on yield stress in BCC HEA

To verify the rationality of this model in BCC HEAs, the yield stress from the theoretical model is compared to the previous experimental data [34,50]. As shown in Fig. 4a, the yield stress of 960 MPa from our model prediction agrees well with that of 1073 MPa [50], and of 929 MPa [34] from the experimental data in the BCC TaNbHfZrTi HEA. The deviation between the predicted and experimental data are less than 10%. In addition, the yield stress is composed of the grain-boundary strengthening of 22 MPa, and the solid-solution strengthening of 938 MPa, suggesting the severe-lattice-distortion-dominated strength, which is different from the strong grain-boundary strengthening in the FCC $Al_{0.3}$CrCoFeNi HEAs.

Fig. 4b shows the relationship between the experimental and predicted yield stresses in various BCC HEAs. It is evident that the computed results of the present model can match well the most of the experimental data in BCC HEAs. For HfNbTaTiZr, MoNbTaW, MoNbTaVW, NbMoTaV, TiMoTaHfZr, and TiNbMoZrHf HEAs, the deviation between the predictions and experimental results are less than 10%. As for the NbTiTaV, TiNbMoTaHfZr, NbWTaV, NbWTaVTi, and TiNbMoTaV HEAs, the deviation between the predicted and experimental results are slightly greater than 10%. In addition, the yield stress of BCC HEAs is also not directly depend on the number of components, which is consistent with the variation tendency of solid-solution strengthening in FCC HEAs.

3.3. Effect of Al fraction in Al_x-Hf-Nb-Ta-Ti-Zr and Al_x-Cr-Co-Fe-Ni-Mn HEAs

To investigate the effect of the Al atomic fraction on the mechanical properties in BCC Al_x-Hf-Nb-Ta-Ti-Zr HEAs, the present model is

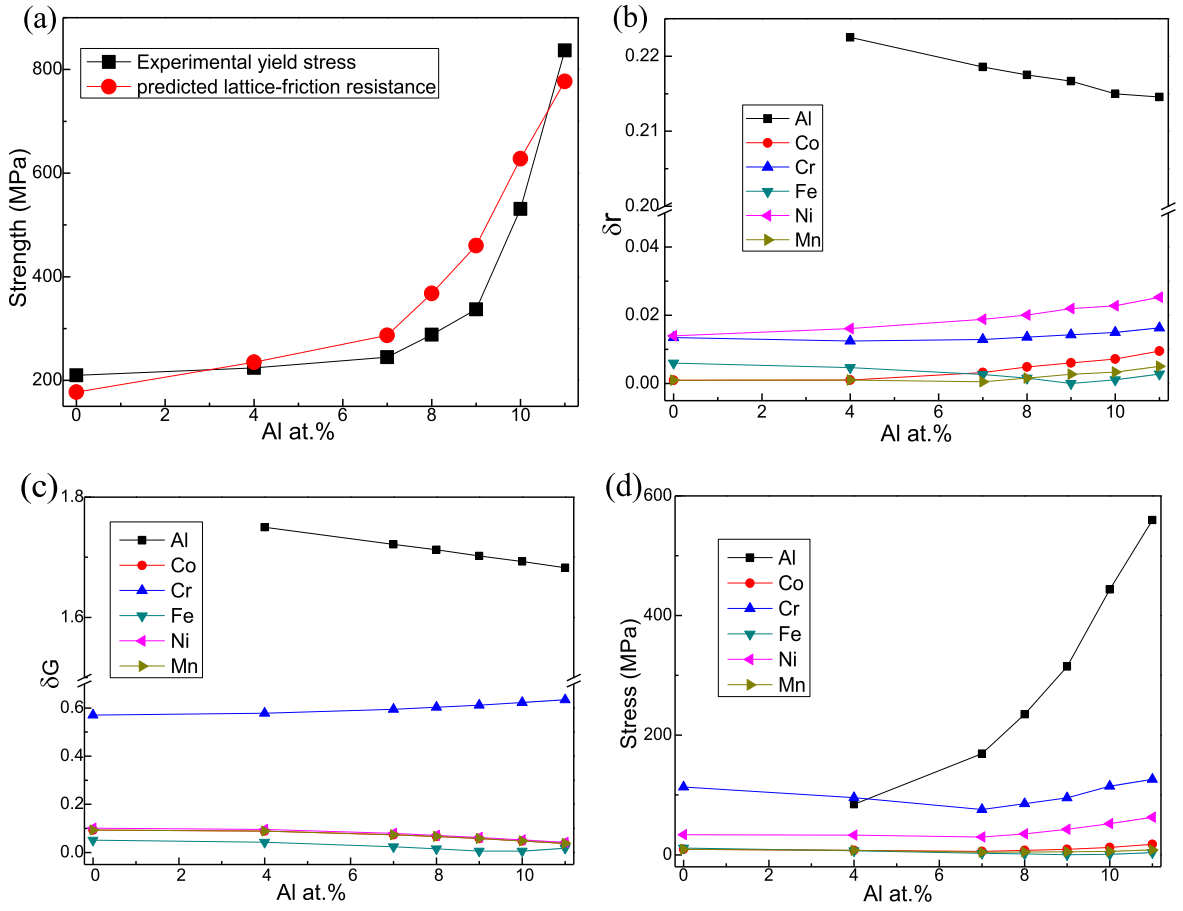

Fig. 6. The relationship between the solid-solution strengthening and Al composition (atomic-size mismatch, shear-modulus mismatch, and solid-solution strengthening) in the Al_x-Cr-Co-Fe-Ni-Mn HEAs.

employed to predict the yield stress for Al_x-Hf-Nb-Ta-Ti-Zr HEAs in the large range from 0 to 1. The previous research indicates that the Al_x-Hf-Nb-Ta-Ti-Zr HEA system exhibits a single BCC crystal structure with the x value in the range of 0–1 [50]. As shown in Fig. 5a, the yield stress predicted by the present model can match well that from the experiment with increasing the Al composition in the Al_x-Hf-Nb-Ta-Ti-Zr HEAs [50]. The deviation between the predicted and experimental results is less than 10%. Moreover, the predicted yield strength of the Al_x-Hf-Nb--Ta-Ti-Zr HEA system increases with the increase of the Al content, agreeing with the previous experiment [50]. For the series of Al_x-Hf-Nb-Ta-Ti-Zr HEAs, all predictions in yield strength are less than experimental data, due to the underestimate of the shear modulus in HEAs. The experimental results show the shear modulus increase with the increasing Al composition in Al_x-Hf-Nb-Ta-Ti-Zr HEAs, but decrease based on Eq. (9). But the proposed model captures the main features of the variation in yield stress with Al concentration in Al_x-Hf-Nb-Ta-Ti-Zr HEAs.

Fig. 5b and c exhibit the atomic-radius mismatch, $|\delta r_i|$, and the shear-modulus mismatch, $|\delta G_i|$, in the Al_x-Hf-Nb-Ta-Ti-Zr HEAs, which are dependent on the Al contents. The atomic-radius mismatch in the Zr and Hf elements is significantly greater than that in other four principal elements at various Al concentrations, and the atomic-radius mismatch for other four principal elements is very close. This is because the radii of the Zr and Hf elements are obviously larger than radii of other four principal elements whose radii are very close between each other. The shear-modulus mismatch for the Ta element is significantly greater than those for other five principal elements at the different Al contents, as shown in Fig. 5c. For the other five principal elements, the shear-modulus mismatch of the Al element is larger than that of other four principal elements, including Hf, Nb, Zr, and Ni. The shear moduli of pure Hf, Nb, Ti, and Zr metals exhibit almost the same value, but that of pure Ta metal element has a significantly large value. By combining the atomic-radius mismatch and shear-modulus mismatch, the solid-solution strengthening contributed from individual elements change as a function of the Al content is shown in Fig. 5d. The solid-solution strengthening contributed from Zr element is largest, and it from the Ti element is smallest, comparing with the solid-solution strengthening contributed from the other four elements in various Al_x-Hf-Nb-Ta-Ti-Zr HEAs. Comparing with Fig. 5b, c and d, it is obvious that the solid-solution strengthening contributed from elements is dominated by the atomic-radius mismatch for Hf, Nb, Ta, and Zr elements. The atomic-radius mismatch and the shear-modulus mismatch of Al both decrease with the increasing Al content, but the solid-solution strengthening contributed from Al element increases with the increasing Al content. This trend is due to the fact that the stress produced by Al element is dominated by the increasing Al concentration.

Moreover, the proposed theoretical model is employed to explore the effect of the Al concentration on the mismatch parameters and mechanical properties in the Al_x-Cr-Co-Fe-Ni-Mn HEAs. The previous research has shown that the crystal structure can transform from the initial single FCC structure to a duplex FCC + BCC structure with the increasing Al concentration [51]. When the value of x is less than 7, the crystal structure of Al_x-Cr-Co-Fe-Ni-Mn HEAs is the single FCC structure. As the value of x increases to greater than 7 but less than 11, the Al_x-Cr-Co-Fe-Ni-Mn present the dual-phase HEAs containing BCC and FCC structure. Fig. 6a exhibits the predicted solid-solution strengthening and corresponding experimental yield stress in the Al_x-Cr-Co-Fe-Ni-Mn HEAs. The yield stress is composed of solid-solution strengthening and

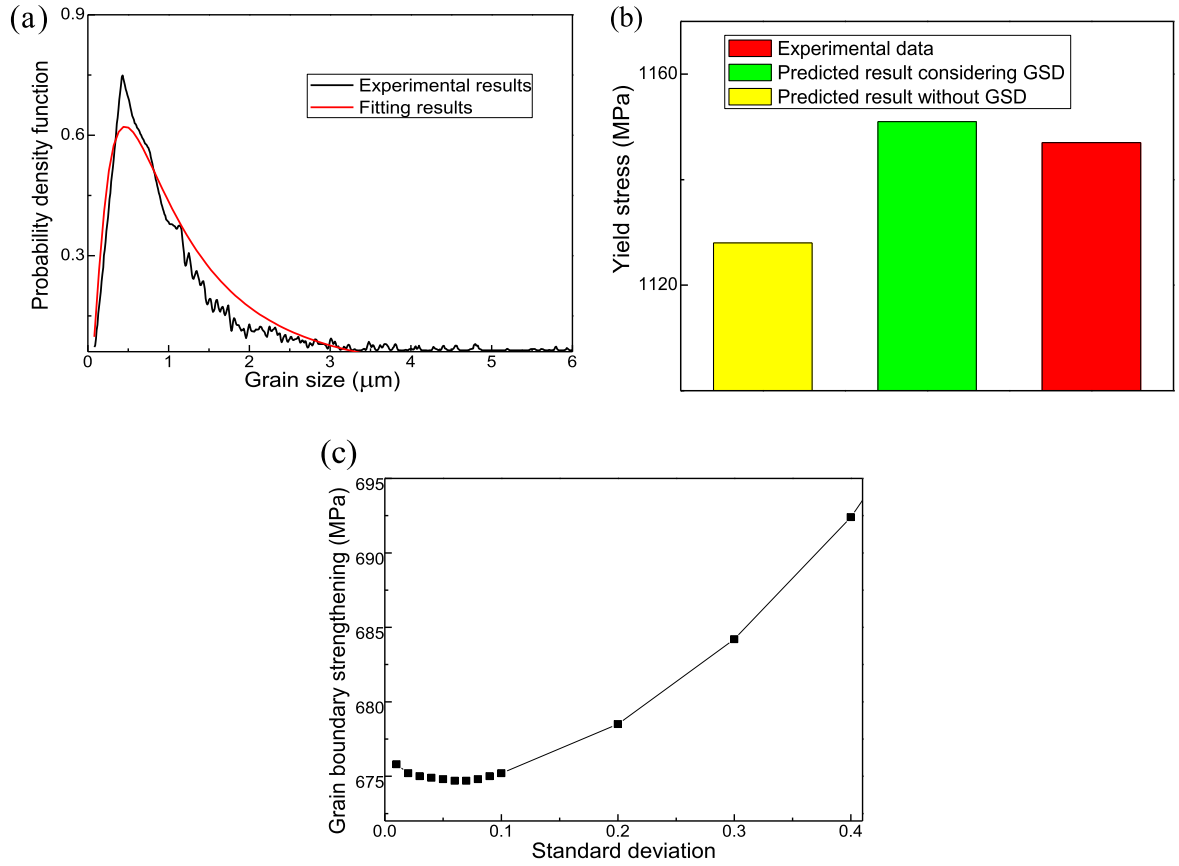

Fig. 7. (a) The probability density function vs. grain size. The black line is the experimental results from previous study [13], the red line represents the fitted results based on the experimental results. (b) The comparison of the yield stresses between the predicted result without the grain size distribution, the predicted result considering the grain-size distribution, and the experimental data for the $Al_{0.3}$CoCrFeNi HEA [13]. (c) The relationship of the grain boundary strengthening and the standard deviation for the grain-size distribution. (For interpretation of the references to color in this figure legend, the reader is referred to the Web version of this article.)

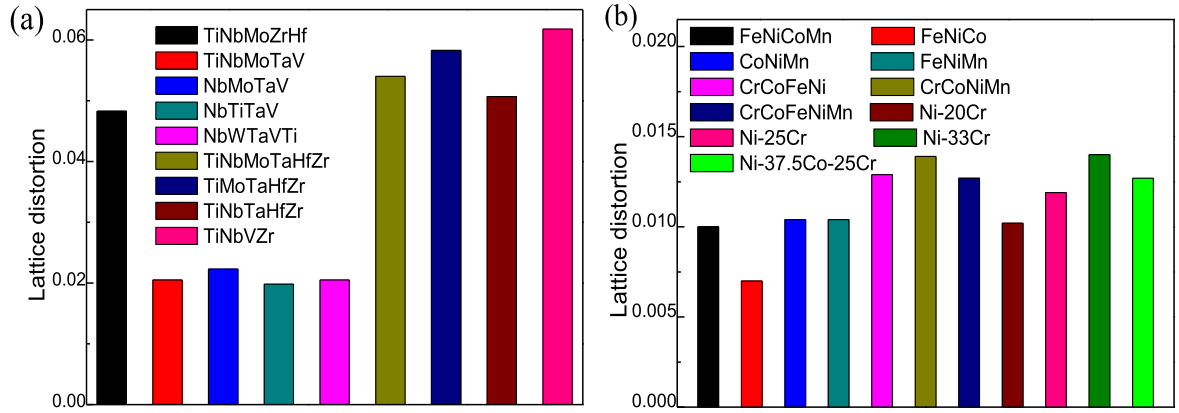

Fig. 8. The comparison of the atomic-radius mismatch in various BCC HEAs [36] (a), FCC HEAs and binary alloys (b).

other strengthening effects. The predictions are in good agreement with the experimental data at various x values. Hence, the presented model acquires the main tendency of the variation in yield stress with the increasing Al concentration and the formation of the BCC phase in Al_x-Cr-Co-Fe-Ni-Mn HEAs.

Fig. 6b, c and d show the atomic-radius mismatch, $|\delta r_i|$, the shear-modulus mismatch, $|\delta G_i|$, and the strengthening introduced by various elements changes with the increase of the Al concentration. The atomic-radius mismatch and the shear-modulus mismatch of Al element are significantly greater than that of the other five elements at all x values, but the strengthening introduced by Al element is close to the strengthening introduced by the other five elements at small x values. With the increase of Al concentration, the strengthening introduced by Al element sharply increases and dominate the solid-solution strengthening in the Al_x-Cr-Co-Fe-Ni-Mn HEAs. The shear-modulus mismatch produced by Cr element is obviously larger than that of Co, Fe, Ni and Mn elements, which govern the strengthening produced by Cr element. As for the Co, Fe, Ni and Mn elements, the atomic-radius mismatch and

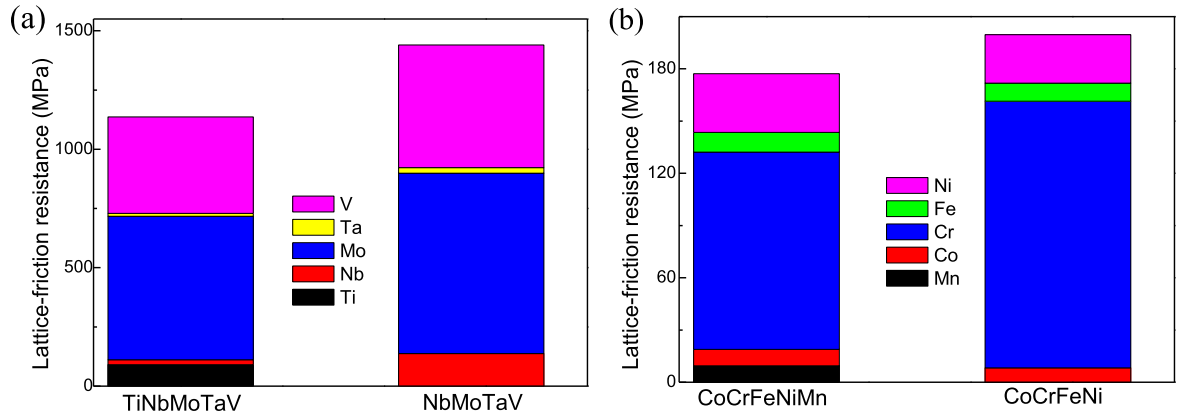

Fig. 9. (a) The comparison of the solid-solution strengthening in the TiNbMoTaV and NbMoTaV BCC HEA [36]. (b) The comparison of the solid-solution strengthening in the CoCrFeNiMn and CoCrFeNi FCC HEA.

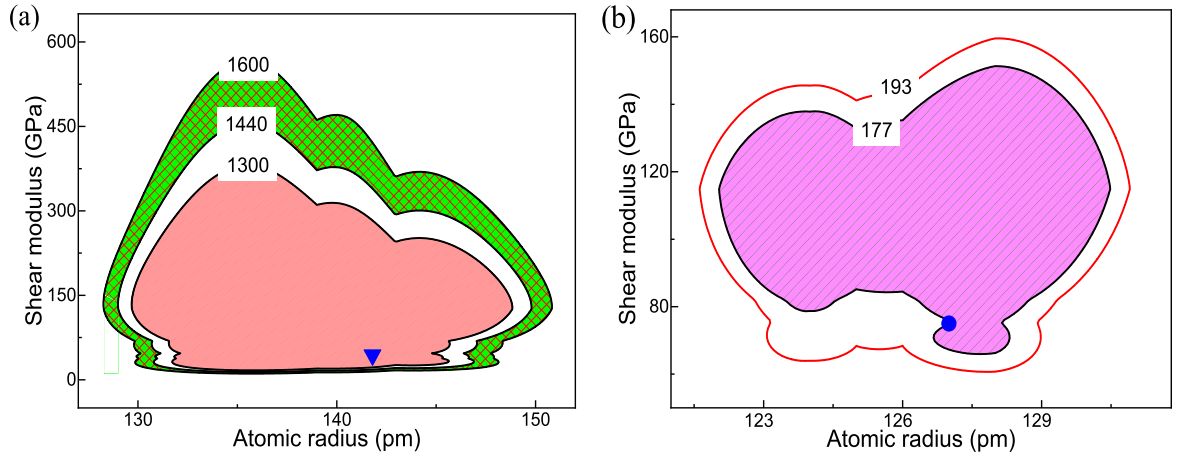

Fig. 10. Parametric analysis on the various atomic radius and shear modulus affecting the solid-solution strengthening in BCC NbMoTaVX HEA (a) and FCC CoCrFeNiX HEA (b).

the shear-modulus mismatch dominate the strengthening together. In Fig. 6d, the strengthening introduced by Co, Cr, Fe, Ni, Mn elements keep almost unchanged or decrease slightly when $x < 7$, this is the result of the competitive mechanism between the mismatch parameters in Fig. 6b and c and reduced concentration of individual elements. With the increasing Al concentration, the strengthening introduced by individual elements all increase remarkably, due to the appearance of the BCC structure. The present research not only catch the variation-tendency of the yield stress with the appearance of the BCC phase, but also identify the effect of the elemental concentration on the solid-solution strengthening in HEAs.

3.4. *Effect of grain size distribution*

The grain-boundary strengthening is 652 MPa in the $Al_{0.3}CoCrFeNi$ HEA, which shows the Hall-Petch coefficient of 824 MPa $\mu m^{0.5}$ and the average grain size of 1.6 μm in the previous work [13,46]. This value is less than the experimental result (Fig. 3a). To solve this issue, the effect of the grain-size distribution on the yield strength is not considered to be negligible. The grain-size distribution in the previous research [13] is fitted in Fig. 7a, where the parameters of μ and σ are 1.6315 and 0.0158 in Eq. (9). Based on the previous work [52], the grain-size interval is taken to be equal to 0.2 μm, and the maximum grain size in the integral is affirmed to 100 μm. The comparison between the predicted result, ignoring and considering the grain-size distribution, and the experimental data is mentioned in Fig. 7b. Concerning the effect of the grain-size distribution, the grain-boundary strengthening is 675 MPa in the current work. Regarding the grain-size distribution, the yield strength about 1151 MPa agrees with the experiment of about 1147 MPa with almost no deviation. Fig. 7c illustrates the grain-boundary strengthening changes as a function of the standard deviation for the change of the grain-size distribution. With increasing the standard deviation, the grain-boundary strengthening firstly decreases, and then increases. For the large standard deviation (Fig. 7c), it means that the HEA composed of many nanograins can enhance its yield strength.

4. Discussion

The previous study shows the atomic-radius mismatch enhances with increasing the number of incorporated principal elements in HEAs [53]. However, it is demonstrated that the lattice strain in CoCrFeMnNi is not significant but similar to that in CrNi and CoCrNi lately [33]. Fig. 8a shows the atomic-radius mismatch in various BCC HEAs based on Eq. (3). It is found that the increasing incorporated principal elements does not necessarily increase the atomic-radius mismatch in HEAs, which is against with the previous work [53]. For example, the atomic-radius mismatch in the four-principal-element TiNbVZr HEA is higher than that in the five-principal-element TaTiMoZrHf HEA. The atomic-radius mismatch in the five-principal-element TaTiMoZrHf HEA is higher than that in six-principal-element TiNbMoTaHfZr HEA (see Fig. 8a). Compared to TaTiMoZrHf HEA, the added Nb element in the TiNbMoTaHfZr HEA reduces the atomic-radius mismatch due to the no obvious

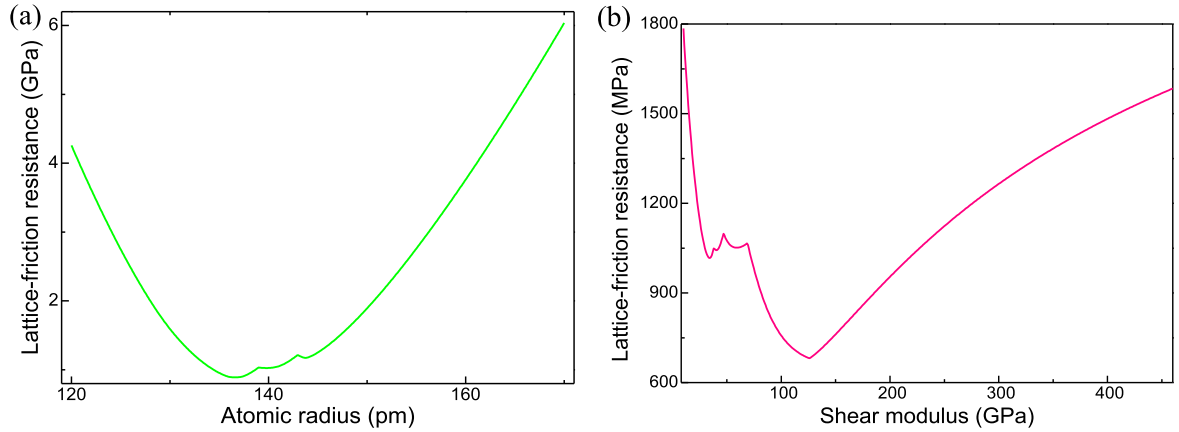

Fig. 11. (a) The relationship between the solid-solution strengthening and atomic radius at a given shear modulus of 38 GPa in NbMoTaVX HEA, which indicates the shear modulus of the added element X is 38 GPa. (b) The relationship between the solid-solution strengthening and shear modulus at a given atomic radius of 140 p. m., which means the atomic radius of the added element X is 140 p.m.

difference in the atomic sizes, compared to other pure metals (r_{Ta} = 0.143 nm, r_{Ti} = 0.142 nm, r_{Nb} = 0.143 nm, r_{Mo} = 0.139 nm, r_{Hf} = 0.154 nm, r_{Zr} = 0.160 nm [34,36]). Therefore, the difference of the atomic sizes determines the atomic-radius mismatch, rather than increasing the number of the incorporated principal elements, to further determine the solid-solution strengthening of HEAs, agreeing with the previous research [32]. Fig. 8b shows the atomic-radius mismatch in various BCC HEAs and binary alloys based on Eq. (3). The result indicates that the atomic-radius mismatch in HEAs and medium-entropy alloys are not significant but similar to that in binary alloys, which is consistent with previous research [33]. Hence, the present research demonstrate the lattice strain in HEAs are not prominent theoretically.

Fig. 9a and b shows the solid-solution strengthening of the TiNbMoTaV series BCC HEAs and the CoCrFeNiMn series FCC HEAs [36]. The solid-solution strengthening of the four-principal-element NbMoTaV HEA is larger than that of five-principal-element TiNbMoTaV HEA. Though the solid-solution strengthening contributed from Ti exist in TiNbMoTaV HEA, the solid-solution strengthening contributed from the other four elements in NbMoTaV HEA are all higher than that in TiNbMoTaV HEA. This is due to the atomic-radius and shear modulus of the added Ti are close to the atomic-radius and shear modulus of the other four elements. In the same way, this situation also happened to the CoCrFeNiMn and CoCrFeNi HEAs, as shown in Fig. 9b.

From our model, it could assess the effect of the atomic radius and shear modulus for the added element in the mechanical properties. The contour plots on the shear modulus and atomic radius effects in solid-solution strengthening are shown in Fig. 10a and b for BCC NbMoTaV and FCC CoCrFeNi HEAs, respectively. The middle contour line represents the 1440 MPa of solid-solution strengthening in NbMoTaV HEAs, revealing the correlation between the atomic radius, shear modulus and the solid-solution strengthening in NbMoTaVX HEAs (Fig. 10a). Here, the element "X" denotes for the various type element. If we want to screen the NbMoTaVX with a solid-solution strengthening less than 1300 MPa, the atomic radius and shear modulus of X should locate in red region. For instance, the blue point in red region represents the atomic radius of 142 p.m. and shear modulus of 44 GPa for Ti element in Fig. 10a, respectively, so the solid-solution strengthening for TiNbMoTaV of 1137 MPa is less than that of NbMoTaV [36]. If the selected NbMoTaVX with a solid-solution strengthening larger than NbMoTaV of 1440 MPa but less than 1600 MPa, the atomic radius and shear modulus of X should locate in green region. Similarly, if the value of atomic radius and shear modulus for the added X element are within the red contour line in Fig. 10b, the solid-solution strengthening of CoCrFeNiX HEAs will be less than the CoCrFeNi of 193 MPa. Therefore, the added X will reduce the solid-solution strengthening of CoCrFeNi HEA. The blue point on the border of the pink region represents the CoCrFeNiMn with a solid-solution strengthening of 177 MPa [47]. If we want to screen the CoCrFeNiX with a solid-solution strengthening less than 177 MPa, the atomic radius and shear modulus of X should locate in pink region. Therefore, our model can provide help for discovering and screening the high strength of advanced HEAs.

Moreover, the interval of shear modulus is significantly higher than that of the atomic radius for both NbMoTaVX and CoCrFeNiX HEAs, as shown in Fig. 10a and b. This trend indicates the fact that the effect of the atomic radius on the solid-solution strengthening is obviously higher than that of the shear modulus. To further confirm this conclusion, the correlation between the solid-solution strengthening and atomic radius at a given shear modulus, and shear modulus at a given atomic radius for NbMoTaVX HEA is shown in Fig. 11a and b. The interval of atomic radius is 50 p.m. in Fig. 11a, the interval of solid-solution strengthening is 5140 MPa. The interval of shear modulus is 450 GPa, but the interval of solid-solution strengthening is only 1100 MPa in Fig. 11b. Comparing Fig. 11a and b, it is obvious the change of solid-solution strengthening caused by the variation of atomic radius is much larger than that caused by shear modulus. This trend indicates that the atomic-radius mismatch governs the mismatch parameter, and further dominate the solid-solution strengthening.

5. Conclusions

The theoretical model coupling the lattice distortion with grain-size distribution is presented to describe the solid-solution strengthening and yield strength in FCC and BCC structured HEAs. The simulated results are in good agreement with the experimental data obtained for the solid-solution strengthening and the yield strength in various HEAs. It has been confirmed the atomic-radius mismatch and solid-solution strengthening can be irrelevant to the increasing number of components in HEAs. In the Al_x-Cr-Co-Fe-Ni-Mn HEA, the solid-solution strengthening is dominated by the atomic-radius mismatch and shear-modulus mismatch introduced by Al element, but the situation does not occur in Al_x-Hf-Nb-Ta-Ti-Zr HEAs. The atomic-radius mismatch has a significantly higher effect on the solid-solution strengthening than that of the shear-modulus mismatch, which further dominate the yield strength. Moreover, the accuracy of the predicted results could improve with the consideration of the grain size distribution. The proposed theoretical model appears to be capable of capturing the main features of the variation in solid-solution strengthening with changing alloy composition and concentration in various HEAs. The present research demonstrate that the atomic-radius mismatch in HEAs and medium-entropy alloys are not significant but similar to that in binary alloys

theoretically. The corresponding contour line of various HEAs can provide help for discovering and screening the high strength of advanced HEAs. Hence, it is believed that the present proposed model can be applied to investigate the severe lattice distortion on HEAs from the theoretical perspective.

Declaration of competing interest

The authors declare that they have no known competing financial interests or personal relationships that could have appeared to influence the work reported in this paper.

CRediT authorship contribution statement

Li Li: Conceptualization, Methodology, Formal analysis, Investigation, Writing - original draft, Writing - review & editing. **Qihong Fang:** Formal analysis, Methodology, Resources, Supervision, Writing - review & editing. **Jia Li:** Investigation, Writing - review & editing, Funding acquisition. **Bin Liu:** Writing - review & editing, Project administration, Funding acquisition. **Yong Liu:** Writing - review & editing, Project administration, Funding acquisition. **Peter K. Liaw:** Resources, Writing - review & editing, Project administration, Funding acquisition.

Acknowledgements

The authors would like to deeply appreciate the support from the Foundation for Innovative Research Groups of the National Natural Science Foundation of China (Grant No. 51621004), the NNSFC (11772122, 51871092, 51625404, 51771232, and 51671217), the Fundamental Research Funds for the Central Universities (531107051151), and the National Key Research and Development Program of China (2016YFB0700300). The research is supported by Hunan Provincial Innovation Foundation for Postgraduate (CX2018B156). PKL would like to acknowledge the Department of Energy (DOE), Office of Fossil energy, National Energy Technology Laboratory (DE-FE-0011194) with the program manager, Dr. J. Mullen. PKL very much appreciates the support of the U.S. Army Research Office project (W911NF-13-1-0438 and W911NF-19-2-0049) with the program managers, Drs. M.P. Bakas, S.N. Mathaudhu, and D.M. Stepp. PKL thanks the support the National Science Foundation (DMR-1611180 and 1809640) with the program directors, Drs. G. Shiflet and D. Farkas.

References

[1] J.W. Yeh, S.K. Chen, S.J. Lin, J.Y. Gan, T.S. Chin, T.T. Shun, C.H. Tsau, S.Y. Chang, Nanostructured high-entropy alloys with multiple principal elements: novel alloy design concepts and outcomes, Adv. Eng. Mater. 6 (2004) 299–303.
[2] Y. Zhang, T.T. Zuo, Z. Tang, M.C. Gao, K.A. Dahmen, P.K. Liaw, Z.P. Lu, Microstructures and properties of high-entropy alloys, Prog. Mater. Sci. 61 (2014) 1–93.
[3] Y. Shi, B. Yang, X. Xie, J. Brechtl, K.A. Dahmen, P.K. Liaw, Corrosion of Al_xCoCrFeNi high-entropy alloys: Al-content and potential scan-rate dependent pitting behavior, Corrosion Sci. 119 (2017) 33–45.
[4] L.J. Santodonato, Y. Zhang, M. Feygenson, C.M. Parish, M.C. Gao, R.J.K. Weber, J. C. Neuefeind, Z. Tang, P.K. Liaw, Deviation from high-entropy configurations in the atomic distributions of a multi-principal-element alloy, Nat. Commun. 6 (2015) 5964.
[5] Z. Tang, T. Yuan, C.W. Tsai, J.W. Yeh, C.D. Lundin, P.K. Liaw, Fatigue behavior of a wrought Al0. 5CoCrCuFeNi two-phase high-entropy alloy, Acta Mater. 99 (2015) 247–258.
[6] Y. Shi, B. Yang, P.K. Liaw, Corrosion-resistant high-entropy alloys: a review, Metals 7 (2017) 43.
[7] M.A. Hemphill, T. Yuan, G.Y. Wang, J.W. Yeh, C.W. Tsai, A. Chuang, P.K. Liaw, Fatigue behavior of Al0.5CoCrCuFeNi high entropy alloys, Acta Mater. 60 (2012) 5723–5734.
[8] D.B. Miracle, O.N. Senkov, A critical review of high entropy alloys and related concepts, Acta Mater. 122 (2017) 448–511.
[9] B. Cantor, I.T.H. Chang, P. Knight, A.J.B. Vincent, Microstructural development in equiatomic multicomponent alloys, Mater. Sci. Eng., A 375 (2004) 213–218.
[10] O.N. Senkov, S.V. Senkova, C.F. Woodward, Effect of aluminum on the microstructure and properties of two refractory high-entropy alloys, Acta Mater. 68 (2014) 214–228.
[11] Y.J. Zhao, J.W. Qiao, S.G. Ma, M.C. Gao, H.J. Yang, M.W. Chen, Y. Zhang, A hexagonal close-packed high-entropy alloy: the effect of entropy, Mater. Des. 96 (2016) 10–15.
[12] R. Soler, A. Evirgen, M. Yao, C. Kirchlechner, F. Stein, M. Feuerbacher, D. Raabe, G. Dehm, Microstructural and mechanical characterization of an equiatomic YGdTbDyHo high entropy alloy with hexagonal close-packed structure, Acta Mater. 156 (2018) 86–96.
[13] D. Li, C. Li, T. Feng, Y. Zhang, G. Sha, J.J. Lewandowski, P.K. Liaw, Y. Zhang, High-entropy $Al_{0.3}$CoCrFeNi alloy fibers with high tensile strength and ductility at ambient and cryogenic temperatures, Acta Mater. 123 (2017) 285–294.
[14] W. Zhang, P.K. Liaw, Y. Zhang, Science and technology in high-entropy alloys, Sci. China Mater. 61 (2018) 2–22.
[15] Y.J. Zhou, Y. Zhang, Y.L. Wang, G.L. Chen, Solid solution alloys of AlCoCrFeNiTix with excellent room-temperature mechanical properties, Appl. Phys. Lett. 90 (2007), 181904.
[16] B. Gludovatz, A. Hohenwarter, D. Catoor, E.H. Chang, E.P. George, R.O. Ritchie, A fracture-resistant high-entropy alloy for cryogenic applications, Science 345 (2014) 1153–1158.
[17] R. Sriharitha, B.S. Murty, Ravi S. Kottada, Alloying, thermal stability and strengthening in spark plasma sintered AlxCoCrCuFeNi high entropy alloys, J. Alloys Compd. 583 (2014) 419–426.
[18] K.Y. Tsai, M.H. Tsai, J.W. Yeh, Sluggish diffusion in Co-Cr-Fe-Mn-Ni high-entropy alloys, Acta Mater. 61 (2013) 4887–4897.
[19] H. Luo, Z. Li, A.M. Mingers, D. Raabe, Corrosion behavior of an equiatomic CoCrFeMnNi high-entropy alloy compared with 304 stainless steel in sulfuric acid solution, Corrosion Sci. 134 (2018) 131–139.
[20] T. Fujieda, H. Shiratori, K. Kuwabara, M. Hirota, T. Kato, K. Yamanaka, Y. Koizumi, A. Chiba, S. Watanabe, CoCrFeNiTi-based high-entropy alloy with superior tensile strength and corrosion resistance achieved by a combination of additive manufacturing using selective electron beam melting and solution treatment, Mater. Lett. 189 (2017) 148–151.
[21] M.H. Chuang, M.H. Tsai, W.R. Wang, S.J. Lin, J.W. Yeh, Microstructure and wear behavior of AlxCo1.5CrFeNi1.5Tiy high-entropy alloys, Acta Mater. 59 (2011) 6308–6317.
[22] M.M. Serna, J.L. Rossi, MC complex carbide in AISI M2 high-speed steel, Mater. Lett. 63 (2009) 691–693.
[23] R. Chen, G. Qin, H. Zheng, L. Wang, Y. Su, Y. Chiu, H. Ding, J. Guo, H. Fu, Composition design of high entropy alloys using the valence electron concentration to balance strength and ductility, Acta Mater. 144 (2018) 129–137.
[24] X.D. Xu, P. Liu, Z. Tang, A. Hirata, S.X. Song, T.G. Nieh, P.K. Liaw, C.T. Liu, M. W. Chen, Transmission electron microscopy characterization of dislocation structure in a face-centered cubic high-entropy alloy Al0. 1CoCrFeNi, Acta Mater. 144 (2018) 107–115.
[25] S. Huang, W. Li, S. Lu, F. Tian, J. Shen, E. Holmström, L. Vitos, Temperature dependent stacking fault energy of FeCrCoNiMn high entropy alloy, Scripta Mater. 108 (2015) 44–47.
[26] J. Li, Q. Fang, B. Liu, Y. Liu, Transformation induced softening and plasticity in high entropy alloys, Acta Mater. 147 (2018) 35–41.
[27] C. Varvenne, A. Luque, W.A. Curtin, Theory of strengthening in fcc high entropy alloys, Acta Mater. 118 (2016) 164–176.
[28] C. Varvenne, G.P.M. Leyson, M. Ghazisaeidi, W.A. Curtin, Solute strengthening in random alloys, Acta Mater. 124 (2017) 660–683.
[29] B. Schuh, F. Mendez-Martin, B. Völker, E.P. George, H. Clemens, R. Pippan, A. Hohenwarter, Mechanical properties, microstructure and thermal stability of a nanocrystalline CoCrFeMnNi high-entropy alloy after severe plastic deformation, Acta Mater. 96 (2015) 258–268.
[30] F. Otto, A. Dlouhý, C. Somsen, H. Bei, G. Eggeler, E.P. George, The influences of temperature and microstructure on the tensile properties of a CoCrFeMnNi high-entropy alloy, Acta Mater. 61 (2013) 5743–5755.
[31] L. Zhang, Y. Xiang, J. Han, D.J. Srolovitz, The effect of randomness on the strength of high-entropy alloys, Acta Mater. 166 (2019) 424–434.
[32] F.G. Coury, M. Kaufman, A.J. Clarke, Solid-solution strengthening in refractory high entropy alloys, Acta Mater. 175 (2019) 66–81.
[33] L.R. Owen, E.J. Pickering, H.Y. Playford, H.J. Stone, M.G. Tucker, N.G. Jones, An assessment of the lattice strain in the CrMnFeCoNi high-entropy alloy, Acta Mater. 122 (2017) 11–18.
[34] O.N. Senkov, J.M. Scott, S.V. Senkova, D.B. Miracle, C.F. Woodward, Microstructure and room temperature properties of a high-entropy TaNbHfZrTi alloy, J. Alloys Compd. 509 (2011) 6043–6048.
[35] Z. Wang, Q. Fang, J. Li, B. Liu, Y. Liu, Effect of lattice distortion on solid solution strengthening of BCC high-entropy alloys, J. Mater. Sci. Technol. 34 (2018) 349–354.
[36] H.W. Yao, J.W. Qiao, J.A. Hawk, H.F. Zhou, M.W. Chen, M.C. Gao, Mechanical properties of refractory high-entropy alloys: experiments and modeling, J. Alloys Compd. 696 (2017) 1139–1150.
[37] R. Labusch, A statistical theory of solid solution hardening, Phys. Status Solidi 41 (1970) 659.
[38] R.L. Fleischer, Substitutional solution hardening, Acta Metall. 11 (1963) 203–209.
[39] L.A. Gypen, A. Deruyttere, Multi-component solid solution hardening, J. Mater. Sci. 12 (1977) 1028–1033.
[40] I. Toda-Caraballo, P.E. Rivera-Díaz-del-Castillo, Modelling solid solution hardening in high entropy alloys, Acta Mater. 85 (2015) 14–23.
[41] H.A. Moreen, R. Taggart, D.H. Polonis, A model for the prediction of lattice parameters of solid solutions, Metall. Trans. 2 (1971) 265–268.

[42] W.H. Liu, Y. Wu, J.Y. He, T.G. Nieh, Z.P. Lu, Grain growth and the Hall-Petch relationship in a high-entropy FeCrNiCoMn alloy, Scripta Mater. 68 (2013) 526–529.
[43] B. Zhu, R.J. Asaro, P. Krysl, R. Bailey, Transition of deformation mechanisms and its connection to grain size distribution in nanocrystalline metals, Acta Mater. 53 (2005) 4825–4838.
[44] S. Berbenni, V. Favier, M. Berveiller, Impact of the grain size distribution on the yield stress of heterogeneous materials, Int. J. Plast. 23 (2007) 114–142.
[45] K. Ma, H. Wen, T. Hu, T.D. Topping, D. Isheim, D.N. Seidman, E.J. Lavernia, J. M. Schoenung, Mechanical behavior and strengthening mechanisms in ultrafine grain precipitation-strengthened aluminum alloy, Acta Mater. 62 (2014) 141–155.
[46] B. Gwalani, V. Soni, M. Lee, S.A. Mantri, Y. Ren, R. Banerjee, Optimizing the coupled effects of Hall-Petch and precipitation strengthening in a $Al_{0.3}$CoCrFeNi high entropy alloy, Mater. Des. 121 (2017) 254–260.
[47] J. Lan, X. Shen, J. Liu, L. Hua, Strengthening mechanisms of 2A14 aluminum alloy with cold deformation prior to artificial aging, Mater. Sci. Eng., A 745 (2019) 517–535.
[48] Z.T. Liu, B.Y. Wang, C. Wang, M. Zha, G.J. Liu, Z.Z. Yang, H.Y. Wang, Microstructure and mechanical properties of Al-Mg-Si alloy fabricated by a short process based on sub-rapid solidification, J. Mater. Sci. Technol. 41 (2020) 178–186.
[49] Z. Wu, H. Bei, G.M. Pharr, E.P. George, Temperature dependence of the mechanical properties of equiatomic solid solution alloys with face-centered cubic crystal structures, Acta Mater. 81 (2014) 428–441.
[50] C.M. Lin, C.C. Juan, C.H. Chang, C.W. Tsai, J.W. Yeh, Effect of Al addition on mechanical properties and microstructure of refractory AlxHfNbTaTiZr alloys, J. Alloys Compd. 624 (2015) 100–107.
[51] J.Y. He, W.H. Liu, H. Wang, Y. Wu, X.J. Liu, T.G. Nieh, Z.P. Lu, Effects of Al addition on structural evolution and tensile properties of the FeCoNiCrMn high-entropy alloy system, Acta Mater. 62 (2014) 105–113.
[52] Q. Fang, L. Li, J. Li, H. Wu, Z. Huang, B. Liu, Y. Liu, P.K. Liaw, A statistical theory of probability-dependent precipitation strengthening in metals and alloys, J. Mech. Phys. Solid. 122 (2019) 177–189.
[53] J.W. Yeh, S.Y. Chang, Y.D. Hong, S.K. Chen, S.J. Lin, Anomalous decrease in X-ray diffraction intensities of Cu-Ni-Al-Co-Cr-Fe-Si alloy systems with multi-principal elements, Mater. Chem. Phys. 103 (2007) 41–46.